



Ionization and electron-capture cross sections for single- and multiple-electron removal from H₂O by Li³⁺ impact

H. Luna,* W. Wolff, and E. C. Montenegro

Departamento de Física, Universidade Federal do Rio de Janeiro Caixa Postal 68528, Rio de Janeiro, 21945-970, RJ, Brazil

André C. Tavares

Departamento de Física, Pontifícia Universidade Católica do Rio de Janeiro, Caixa Postal 38071, 22452-970, RJ, Brazil

H. J. Lüdde

Institut für Theoretische Physik, Goethe-Universität, D-60438 Frankfurt, Germany

G. Schenk, M. Horbatsch, and T. Kirchner[†]

Department of Physics and Astronomy, York University, Toronto, Ontario, Canada M3J 1P3

(Received 15 March 2016; published 13 May 2016)

In this work, we report experimental and theoretical ionization and electron-capture cross sections for single-, double- and triple-electron removal from H₂O by Li³⁺ impact at energies ranging from 0.75 to 5.8 MeV. The experiment was carried out by selecting both the final charge state of the projectile and the ejected fragments in coincidence to obtain cross sections associated with ionization and electron-capture channels. The ionic fragments and the emitted electrons produced under single-collision conditions were collected by a time-of-flight spectrometer with single-hit (e.g., OH⁺ + H⁰) and double-hit events (e.g., OH⁺ + H⁺) properly discriminated. For the one- and two-electron removal cases, the calculations based on the basis generator method for orbital propagation agree well with the experiment for most of the collision channels studied. Auger-electron emission after vacancy production in the inner 2*a*₁ orbital of H₂O is shown to have a substantial effect on the final charge-state distributions over the entire impact-energy interval.

DOI: [10.1103/PhysRevA.93.052705](https://doi.org/10.1103/PhysRevA.93.052705)

I. INTRODUCTION

The study of collisions between heavy ions and water molecules has received great attention in recent decades due to the clinical use of heavy ions in the treatment of tumors [1–3]. This motivation has created the side effect of making water a benchmark molecule to understand the collision dynamics of heavy ions impinging on multielectron molecular systems, and a variety of ions with different charge states have been studied to this end in recent years.

For protons, since the total cross-section measurements reported by Rudd *et al.* [4], there have been several differential and total cross-section studies for ionization [5–9], electron capture [6], electron emission [10], and kinetic-energy releases (KERs) [11–13] covering a wide range of projectile energies. The situation is similar for helium ions as projectiles, where cross sections for ionization [5,14,15], electron capture, transfer ionization [6,14–17], and KERs [18–20] have been measured for both of its ionic charge states.

The case of heavier ions is considerably different because of the large range of charge states which can be involved. Depending on the combination of projectile energy and charge state, very different collision regimes can be reached, inhibiting a general description using one common conceptual approach or approximation level. The observation of collision channels other than ionization, such as electron capture and

electron loss, becomes essential for understanding the collision dynamics. Moreover, as a general rule, collisions with multiply charged ions are quite violent, dissociating the molecules into multiple fragments with different ionic states, some of which have relatively large kinetic energies. For all of these reasons, the experimental arrangements usually have a specific focus, since it is very difficult to obtain a complete characterization of the entire kinematical and dynamical ranges with the same experimental setup. Examples of the efforts made in this direction are KER measurements for low-energy F⁺ [13], Xe²²⁺ [2], and Ne^{*q*+} [21], or for Ni²⁵⁺ ions at high energies [22], electron emission cross sections for swift C⁶⁺ [23] and O⁸⁺ [24] impact, or selective electron capture by O⁶⁺ [25] at low velocities. Absolute cross-section measurements for fragment-ion production, separating ionization, electron-loss, and electron-capture channels, are quite scarce. To the authors' knowledge, the only collision systems studied involve C⁰ and C⁺ with energies between 20 and 100 keV [26], C³⁺ and O⁵⁺ with energies in the 1–3.5 MeV range [27], and Xe⁴⁴⁺ at 6.7 MeV/u [28]. These absolute cross sections are needed for comparison to aid the development of theoretical methods for the collision dynamics over a wide range of projectile energies, as well as for providing reliable input data in simulations of the penetration and damage of heavy ions in water-based environments.

Several theoretical approaches have been used to describe the various channels and features of the collision dynamics of heavy ions with water. Among them are the classical-trajectory Monte Carlo method for ionization, electron capture, and electron emission, covering a wide range of projectile energies,

*hluna@if.ufrj.br

[†]tomk@yorku.ca

masses, and charge states [29–33], the plane-wave Born approximation for electron emission by swift He^+ and He^{2+} [34], continuum distorted-wave with eikonal initial-state models for electron emission [24], or fragment-ion production [28] and the electron nuclear dynamics approach for electron capture and KER distributions [17].

In the case of highly charged ions, the use of nonperturbative approaches is essential for describing the collision dynamics in the intermediate-velocity regime. Moreover, as there is a strong coupling between at least two of the ionization, electron-capture, and electron-loss channels, the concurrent inclusion of these channels in the theory is necessary. Recently, a nonperturbative, quantum-mechanical approach to ion-molecule collisions in the independent-electron model (IEM) framework using the basis generator method was applied to single-ionization, single-capture [35], and multiple-electron removal by proton [36,37] and He^+ impact [38]. This approach is extended to Li^{3+} projectiles in the present work.

The dynamics involving multiply charged heavy ions has several features that are absent in the case of lighter projectiles and which play a major role in practical situations. Due to charge-exchange collisions, heavy ions become necessarily dressed along their paths through matter, reaching an energy-dependent equilibrium charge state even if they were initially produced as bare ions.

While at high energies a parametrization through the net projectile charge is sufficient to describe the ionization strength and the ejection of electrons, at intermediate-to-low velocities dressed ions show some dynamical peculiarities which are not present for bare ions. Indeed, it was found that the incomplete electronic screening at small internuclear distances increases the effective projectile charge in a dynamic way, which depends on the momentum transfer [39–42]. Furthermore, the projectile electrons affect the outcome of a collision not only through static screening; they may play an active role and influence even target ionization cross sections in which the final projectile charge state equals the initial one through transfer-ionization processes [43]. As the effective projectile charge state increases, the system deviates more and more from the perturbative regime, up to the limit of the bare projectile. These studies have shown that the availability of experimental absolute cross sections for bare, multiply charged ions is an important requisite for the development of models to describe dressed projectiles with the same charge state in the intermediate-to-low velocity regime.

Absolute measurements of multiple-electron removal differential in the ionization, electron-capture, transfer-ionization, or electron-loss channels using recoil-ion spectroscopy are more elaborate in the case of molecules as compared to atoms. The removal of one or several electrons from an atom produces a single ion in the corresponding charge state. In contrast, the removal of more than one electron from a molecule usually results in fragmentation producing several ionic fragments that must be detected simultaneously in order to reconstruct the original charge state as well as to obtain the absolute cross section for a given mechanism.

As in the atomic case, the determination of the fragment-ion cross sections can be achieved by recording the uncorrelated arrival of the recoil ions in the detector (single hit). However, comparison of these cross sections with theoretical

calculations for multielectron processes involves two steps: (i) the calculation of the cross section for one- or several-electron removal, and (ii) the determination of the fragmentation fractions resulting from the relaxation of the molecular ion after the collision. Notwithstanding recent work in which the fragmentation fractions are determined theoretically [44], most of the information available for these fractions is semiempirical in nature and associated with the production of single vacancies (single-electron removal) in various molecular orbitals (MOs) of the water molecule [28,45,46]. Since in collisions with multiply charged ions some important collision channels are associated with multiple-electron removal (e.g., transfer ionization), the use of this methodology becomes unsuitable to study these channels. For this reason, the recording of the correlated arrival of the fragment ions in the detector (multihit) is needed to obtain multiple-electron removal cross sections directly.

In this work, we report experimental and theoretical direct ionization and electron-capture cross sections for single-, double- and triple-electron removal from water molecules by Li^{3+} impact at energies ranging from 0.75 to 5.8 MeV. The experiment selects the final charge state of the projectile and the ejected fragments in coincidence to obtain the cross sections associated with the ionization and electron-capture channels. The ionic fragments and the emitted electrons produced under single-collision conditions are used to discriminate one-electron removal (e.g., $\text{OH}^+ + \text{H}^0$ production) and two-electron removal (e.g., $\text{OH}^+ + \text{H}^+$ production) events using multihit detection electronics.

The calculations span the somewhat larger energy interval from 0.14 to 7 MeV (corresponding to $E_P = 20\text{--}1000$ keV/u) and are carried out in the IEM framework using the molecular version of the two-center basis generator method (TC-BGM) for orbital propagation. Compared to previous studies for proton and He^+ -ion impact on water molecules [36–38], the present calculations differ in two respects: (i) A larger number of projectile states are included in the basis in order to allow for capture into highly excited Li^{2+} states. (ii) Auger-electron emission after $2a_1$ vacancy production is considered because electron removal from this inner H_2O orbital turns out to be substantial for Li^{3+} impact.

The layout of the paper is as follows. The experimental setup and cross-section measurements are described in Sec. II. We give a brief summary of the absolute total charge-exchange measurements using the growth-rate method in Sec. II A and then provide some details on the partial cross-section measurements in Sec. II B. This is followed by a discussion of the theoretical approach and results in Sec. III. We first summarize the TC-BGM collision calculation in Sec. III A and then describe the statistical model used to account for postcollision Auger emission in Sec. III B. Theoretical and experimental total cross-section results are compared in Sec. IV. We begin in Sec. IV A with a look at the total capture cross sections and discuss the partial, charge-state-correlated cross sections in Sec. IV B. A scaling rule for ionization cross sections that illustrates the validity and limitations of first-order perturbation theory is examined in Sec. IV C. The paper ends with a short summary in Sec. V. Atomic units characterized by $\hbar = m_e = e = 4\pi\epsilon_0 = 1$ are used unless otherwise stated.

II. EXPERIMENTAL SETUP AND RESULTS

The experimental setup used in this work has been described previously [9,47] and only the most important features will be given here. The experiments were carried out at the Pelletron accelerator facility at the Physics Institute of the Rio de Janeiro Federal University. Briefly, a Li^{3+} beam with energies ranging from 750 up to 5900 keV is obtained. The ion beam is then mass, energy, and charge selected by a switching magnet and directed toward the projectile-target collision beam line. The collision beam line is composed of two sets of collimation slits, and three high vacuum chambers placed in tandem. The first one contains a gas cell target used to measure absolute total cross sections. The second one contains an effusive jet target coupled to a time-of-flight mass spectrometer, and it is used for partial cross-section measurements. Finally, a third chamber is used to detect the main ion beam and its products generated from interactions with either the gas cell or the effusive jet target.

After collimation, the ion beam is directed to the gas cell chamber by a horizontal electrostatic deflector, passing through the 2.5 mm entrance and the 3.0 mm exit apertures. Behind this chamber, a second vertical electrostatic deflector is used to discriminate the emerging projectile charge states after the collision with the target gas cell, when measurements of the total absolute charge-exchange cross sections are performed, or to align horizontally the main beam with the time-of-flight spectrometer in the interaction jet chamber, when partial cross sections are measured (in this case, the gas cell is not used and is kept at high vacuum, and vice versa).

A. Absolute total charge-exchange cross sections

The absolute charge-exchange cross sections leading to single- and double-electron capture are determined using the standard growth-rate method [48,49] in the gas cell chamber. This method consists of measuring the growth rate of the emergent fractions of the incident beam, which undergoes charge-exchange collisions, as a function of the gas target density at pressures low enough to ensure single-collision conditions. The experimental procedures performed in this work are the same as those described in detail by Wolff *et al.* [41,47]. The main sources of uncertainties of the measured cross sections are effective collision length, linear least-squares fit to the observed data, zero drift and fluctuations in the capacitance manometer, and collection efficiencies of the projectiles. Combining all of these uncertainties, typical values were estimated to be within 10–20%. The total single- and double-electron-capture cross-section results are summarized in Table I.

B. Absolute partial pure ionization and electron-capture cross sections

1. Coincidence setups and measured collision channels

For the measurement of absolute partial cross sections a time-of-flight mass spectrometer (TOFMS) coupled to an effusive gas-jet assembly is used. The jet assembly is formed by a hypodermic needle coupled to an XYZ motion manipulator. The longitudinal (Y) direction is parallel to the beam, and the transverse, horizontal (X), and vertical (Z)

TABLE I. Total single-capture cross section σ_{SC} and total double-capture cross section σ_{DC} for Li^{3+} - H_2O collisions in Mb, obtained with the growth-rate method.

Energy (keV)	σ_{SC}	σ_{DC}
750	350 ± 36	55 ± 6
1000	230 ± 24	17 ± 2
1500	117 ± 11	11 ± 2
2000	73 ± 8	3.4 ± 0.6
3000	25 ± 3	0.5 ± 0.1
4000	10 ± 1	
5000	5.6 ± 0.6	
5800	3.3 ± 0.4	

directions are perpendicular to the beam. The X direction is defined along the axis of the spectrometer while the Z direction is defined by the direction of the gas jet. Figure 1 shows a sketch of the experimental setup placed in the second interaction chamber.

A third electrostatic deflector is placed right behind the interaction-chamber exit aperture. After colliding with the target gas, the main projectile beam and the formed product beams are separated by charge state by the electrostatic deflector and directed to the projectile-ion detectors. For ion detection, three detectors were used: a position-sensitive resistive anode detector (PS), a surface barrier detector (SB), and a dynode-channel electron multiplier (DT). A Faraday cup was also added for monitoring the high-intensity beam. On the first detector (PS), all projectile charge states were observed simultaneously. The PS consists of two microchannel plates in a chevron configuration with an active diameter of 38 mm and a resistive anode. In the second detector (SB), only one charge state of the emerging projectile ions is detected

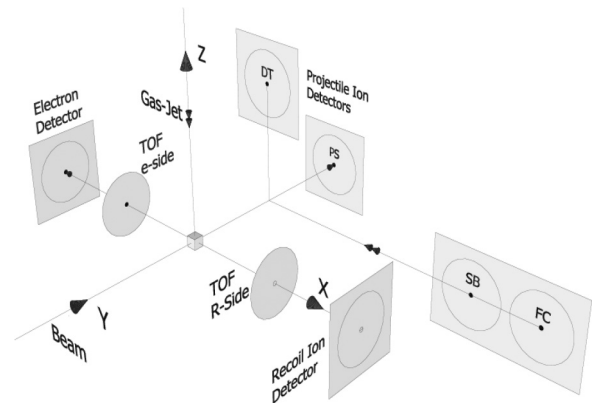


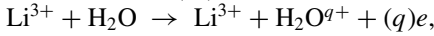
FIG. 1. Coordinate system for the coincidence experiment in the gas-jet assembly. The positive X axis is defined in the axial direction of the spectrometer toward the recoil detector, the positive Y direction along the beam direction, and the negative Z direction in the direction of the gas jet. The electron, recoil-ion, and projectile-ion detectors indicated as SB (surface barrier detector), PS (position-sensitive detector), DT (dynode time-of-flight detector), FC (Faraday cup), and the TOFMS (e-side for electron side and R-side for recoil side) are included in the figure for clarity. The double arrows indicate the movement direction of the detectors.

at a time. The SB is a large area surface detector with an active diameter of 12 mm. A specific projectile charge state is selected by adjusting the voltage applied to the parallel-plate deflector placed after the interaction chamber and directed toward the center of the SB detector. The recoils are directed to a drift tube and detected by two microchannel plates in a chevron configuration. The extracted electrons are focused by an Einzel-lens assembly toward a channel electron multiplier (CEM).

The partial cross sections are obtained by recording (i) the target recoil ions produced by the collision, (ii) the electrons ejected from the target, and (iii) the main beam and its products (i.e., the projectiles). The time-of-flight spectra are determined by two simultaneous coincidence setups to measure (i) coincidences between electrons and recoil ions, and (ii) coincidences between recoil ions and the selected projectile charge state. The output pulses provide the start and stop signals to a multihit coincident setup composed of a fast time-to-digital converter (TDC). A detailed description of the time-of-flight spectrometer is provided in Ref. [47].

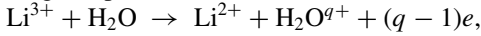
For each projectile energy, three collision channels are measured as follows.

Pure ionization (PI):



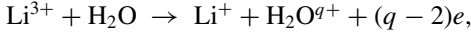
which is composed of single ionization ($q = 1$) and multiple ionization ($q \geq 2$).

Single capture (SC):



which is composed of one-electron capture without target ionization ($q = 1$) and one-electron capture plus target ionization ($q \geq 2$).

Double capture (DC):



which is composed of two-electron capture without target ionization ($q = 2$) and two-electron capture plus target ionization ($q \geq 3$).

The partial cross sections are obtained using a similar approach as described in Ref. [47] for the ionization of He and Ne atoms. The major difference resides in the determination of the recoil-ion detection efficiencies, which are different for molecules and atoms.

For an atomic target, the detection efficiency ϵ_q of a recoil ion of charge $q = 1$ or $q \geq 2$ can be assumed to be independent of the charge state q provided that the recoil-ion detector is working in the plateau regime, i.e., the detector operates in a mode where the efficiency is independent of the recoil-ion mass and charge state and in this case also of the recoil-ion energy prior to detection. Then, a mean efficiency $\bar{\epsilon}$ can be used to describe all recoil charge states [47].

In the case of the water molecule, electron removal (H_2O^{q+} production with $q \geq 1$) leads to the formation of intermediate states. Some of these states are unstable and dissociate rapidly into (i) a single charged fragment plus a neutral fragment (single-ion channels), or (ii) into two (or three) charged fragments (ion-pair and ion-triple channels). In the ion-pair channels, e.g., in $\text{H}_2\text{O}^{2+} \rightarrow \text{H}^+ + \text{OH}^+$, in contrast to the single-ion channels, the detection efficiency must include two single-ion detections instead of the detection of only one (doubly charged) ion. The production of two single ions can lead to a scenario where (at least) one of the produced ions

H^+ or OH^+ is not detected. When this happens, a $q = 2$ event will be measured as a $q = 1$ event, producing an artificial enhancement of the single-ion channels $\text{H}_2\text{O}^+ \rightarrow \text{H}^+ + \text{OH}$ or $\text{H} + \text{OH}^+$. The lower the detection efficiency, the larger this enhancement will be. Therefore, it is necessary to correct the measured yields to obtain the corrected cross sections.

2. Yield-efficiency correction

The procedure used in this work to evaluate the true yields of single-ion and ion-pair fragment production is similar to what was presented in the works of Ben-Itzhak *et al.* [50] and Tavares *et al.* [9]. The efficiency considered is the single-ion detection efficiency ϵ_i , which is assumed to depend only on the recoil-ion detector (multichannel plate, MCP) characteristic. The index i is used to take into account different ion masses and charge states.

The single-ion detection efficiencies ϵ_i can be well approximated by a mean efficiency $\bar{\epsilon}$ if the detection efficiency is independent of the recoil-ion energy and mass [47]. The latter has been realized by measuring the ionization of noble gases and increasing the voltage in the front grid of the MCP up to the point where the ratios $\text{Ne}^{2+}/\text{Ne}^+$ and $\text{Ne}^{3+}/\text{Ne}^+$ become constant. For consistency, we compared the ratios $\text{Ne}^{2+}/\text{Ne}^+$, $\text{Xe}^{2+}/\text{Xe}^+$, and $\text{Ar}^{2+}/\text{Ar}^+$ for ionization by 2 MeV protons with the data available in the literature and obtained good agreement [51,52].

The corrected ion-production yields are obtained by correcting the measured yields for the detection and transmission efficiencies. For the single-ion $\text{OH}^+ + \text{H}$ channel, the corrected yield Y^{corr} can be written as

$$Y^{\text{corr}}(\text{OH}^+ + \text{H}) = \frac{Y^{\text{meas}}(\text{OH}^+ + \text{H})}{\bar{\epsilon}} - \frac{\bar{\epsilon}(1 - \bar{\epsilon})}{\bar{\epsilon}} Y^{\text{corr}}(\text{H}^+ + \text{OH}^+), \quad (1)$$

where $Y^{\text{corr}}(\text{H}^+ + \text{OH}^+)$ is the corrected yield for $\text{H}^+ + \text{OH}^+$ production,

$$Y^{\text{corr}}(\text{H}^+ + \text{OH}^+) = \frac{Y^{\text{meas}}(\text{H}^+ + \text{OH}^+)}{\bar{\epsilon}^2}. \quad (2)$$

The probability of detecting only the OH^+ ion from the $\text{H}^+ + \text{OH}^+$ ion pair is denoted by $\bar{\epsilon}(1 - \bar{\epsilon})$, where it takes into account the detection of a single OH^+ ($\bar{\epsilon}$) constrained to the lack of detection of the transmitted fast H^+ ($1 - \bar{\epsilon}$).

Similar sets of equations can be formulated for the (O^+ , O^{2+} , and O^{3+}) + neutrals single-ion yields and for the ($\text{H}^+ + \text{O}^+$), ($\text{H}^+ + \text{O}^{2+}$), and ($\text{H}^+ + \text{O}^{3+}$) ion-pair yields. For the production of H_2O^+ and H^+ ions, the corrected yields are

$$Y^{\text{corr}}(\text{H}_2\text{O}^+) = \frac{Y^{\text{meas}}(\text{H}_2\text{O}^+)}{\bar{\epsilon}} \quad (3)$$

and

$$Y^{\text{corr}}(\text{H}^+) = \left[\frac{Y^{\text{meas}}(\text{H}^+)}{\bar{\epsilon}} \right] - \left[\frac{\bar{\epsilon}(1 - \bar{\epsilon})}{\bar{\epsilon}^3} \right] \times \left[Y^{\text{meas}}(\text{H}^+ + \text{OH}^+) + \sum_q Y_q^{\text{meas}}(\text{H}^+ + \text{O}^{q+}) \right]. \quad (4)$$

These sets of equations should be written for all three collision channels studied in this work, i.e., PI, SC, and DC. The corrected ion-production yields can be calculated provided $\bar{\epsilon}$ is known.

The value for $\bar{\epsilon}$ is obtained from the DC channel, which involves at least two-electron removal. Hence, the channels involving single-ion production do not contribute and the corrected yield for single-ion production, $Y^{\text{corr}}(\text{OH}^+ + \text{H})$, can be assumed to be zero. Substituting Eq. (2) into Eq. (1) and using the measured values of $Y^{\text{meas}}(\text{OH}^+ + \text{H})$ and $Y^{\text{meas}}(\text{OH}^+ + \text{H}^+)$, an equation involving $\bar{\epsilon}$ is obtained.

For completeness, the procedure is extended to deal with the O^+ , O^{2+} , and O^{3+} yields in the DC channel, assuming that the removal of at least two electrons will always be accompanied by at least one H^+ ion. Following the procedure described above, an average value of $\bar{\epsilon} = 0.17 \pm 0.02$ is obtained from the energies measured for the double-capture channel, and used for all measured projectile energies.

Once the corrected ion-production yields are determined, the partial cross sections are obtained following the normalization procedure to the absolute total electron-capture cross sections described in Refs. [9,47].

3. Cross-section values

The cross sections for each collision channel (PI, SC, DC) are obtained from the corrected yields for target single-ion and ion-pair production as follows.

(i) Single-ion production:

- (i.1) H_2O^+
- (i.2) $\text{OH}^+ + \text{H}$
- (i.3) $\text{O}^+ + 2\text{H}$
- (i.4) $\text{H}^+ + \text{neutrals}$

(ii) Ion-pair production:

- (ii.1) $\text{H}^+ + \text{OH}^+$
- (ii.2) $\text{H}^+ + \text{O}^+$
- (ii.3) $\text{H}^+ + \text{O}^{2+}$
- (ii.4) $\text{H}^+ + \text{O}^{3+}$

The absolute partial cross sections are grouped for each collision channel according to the degree of target ionization. The partial, charge-state-correlated cross sections are denoted by the indices k and l , i.e., σ_{kl} is the partial cross section for finding k electrons transferred from the target to the projectile and l electrons emitted from the target to the continuum. The sum $k + l$ is equal to the degree of target ionization.

PI:

($q = 1$) single ionization - σ_{01} : (i.1) + (i.2) + (i.3) + (i.4) ion production,

($q = 2$) double ionization - σ_{02} : (ii.1) + (ii.2) ion production,

($q = 3$) triple ionization - σ_{03} : (ii.3) ion production,

($q = 4$) quadruple ionization - σ_{04} : (ii.4) ion production.

SC plus transfer ionization:

($q = 1$) single capture - σ_{10} : (i.1) + (i.2) + (i.3) + (i.4) ion production,

($q = 2$) transfer ionization - σ_{11} : (ii.1) + (ii.2) ion production,

($q = 3$) transfer ionization - σ_{12} : (ii.3) ion production,

($q = 4$) transfer ionization - σ_{13} : (ii.4) ion production.

TABLE II. Partial pure-ionization cross sections for Li^{3+} - H_2O collisions in Mb.

Energy (keV)	σ_{01}	σ_{02}	σ_{03}
750	488 ± 70	53 ± 8	4.5 ± 0.8
1000	803 ± 108	152 ± 21	16 ± 3
1500	738 ± 110	148 ± 25	20 ± 4
2000	779 ± 113	133 ± 19	17 ± 4
3000	827 ± 114	130 ± 20	11 ± 4
4000	845 ± 109	103 ± 14	9.1 ± 1.7
5000	900 ± 112	91 ± 12	7.2 ± 1.7
5800	701 ± 92	67 ± 9	4.8 ± 1.3

DC plus transfer ionization:

($q = 2$) double capture - σ_{20} : (ii.1) + (ii.2) ion production,

($q = 3$) transfer ionization - σ_{21} : (ii.3) ion production,

($q = 4$) transfer ionization - σ_{22} : (ii.4) ion production.

It is important to note that the channels (i.4) for $q = 1$, (ii.2) for $q = 2$, (ii.3) for $q = 3$, and (ii.4) for $q = 4$ are contaminated, respectively, by the $\text{H}^+ + \text{H}^+ + \text{O}^{0+,2+,3+}$ channels, since the detector is not able to distinguish between the detection of one H^+ or two simultaneous H^+ .

The measured cross sections are summarized in Tables II, III, and IV for PI, SC, and DC, respectively.

III. THEORETICAL METHODS AND RESULTS

A. Collision calculation

The theoretical framework is a continuation of previous work for the singly charged ion impact on water molecules, which is described in detail in Refs. [35,36,53]. Accordingly, only a brief summary is provided here. We assume that the projectile moves on a classical straight-line trajectory, while the nuclei of the target molecule remain fixed to their equilibrium configuration throughout the collision, i.e., we neglect rovibrational motion. This is well justified for the impact-energy range from 20 to 1000 keV/u considered in this work. The electronic Hamiltonian is assumed to be nonrelativistic and of single-particle form such that the time-dependent Schrödinger equation separates into a set of single-particle equations for the initially populated MOs. The latter are taken from the minimal-basis-set self-consistent-field calculation of Ref. [54].

TABLE III. Partial single-capture cross sections for Li^{3+} - H_2O collisions in Mb.

Energy (keV)	σ_{10}	σ_{11}	σ_{12}
750	126 ± 14	173 ± 20	51 ± 7
1000	69 ± 9	123 ± 15	36 ± 5
1500	26 ± 5	68 ± 9	24 ± 4
2000	9.5 ± 1.6	47 ± 6	17 ± 3
3000	5.3 ± 0.8	15 ± 2	5.9 ± 0.8
4000	1.7 ± 0.3	6.3 ± 0.8	2.4 ± 0.4
5000	0.81 ± 0.1	3.5 ± 0.5	1.3 ± 0.2
5800	0.51 ± 0.07	2.0 ± 0.3	0.84 ± 0.14

TABLE IV. Partial double-capture cross sections for Li^{3+} - H_2O collisions in Mb.

Energy (keV)	σ_{20}	σ_{21}	σ_{22}
1000	5.1 ± 0.8	8.4 ± 1.3	3.8 ± 0.7
1500	3.7 ± 0.6	4.6 ± 0.6	2.2 ± 0.4
2000	1.0 ± 0.2	1.6 ± 0.3	0.70 ± 0.12
3000	0.13 ± 0.02	0.21 ± 0.03	0.11 ± 0.02

This standard IEM framework for heavy-particle collisions is complicated by the occurrence of multicenter matrix elements associated with the molecular Hamiltonian. In order to avoid their explicit calculation, we work in an energy representation and use a single-center expansion of the MOs in terms of an atomic oxygen basis that includes all states of the KLM shells. This representation is incomplete, but has been shown to be sufficient to give reasonable cross-section results for proton and He^+ -ion collisions over a wide range of impact energies spanning from 20 keV/u to several MeV/u [35–38].

A prerequisite for the success of this approach is an accurate and efficient propagation method for the active orbitals. The coupled-channel TC-BGM, which was originally developed for the description of ion-atom collisions, has turned out to be well suited for this task. We use a TC-BGM basis that consists of sets of bound projectile and BGM pseudostates in addition to the atomic oxygen basis that represents the MOs. As in our previous works, we include 22 pseudostates to represent the continuum, but unlike for singly charged ion impact, the (hydrogenlike) projectile states of the first four shells are not sufficient to describe electron transfer to bare lithium ions. For the results presented in this article, we went up to $n = 8$.

The TC-BGM calculations are carried out for the two orientations of the water molecule with respect to the projectile beam axis, which are depicted in Fig. 2. For all of the cross sections reported below, the angle average of these two orientations has been taken. This minimal averaging procedure was demonstrated to give satisfactory cross-section results [35].

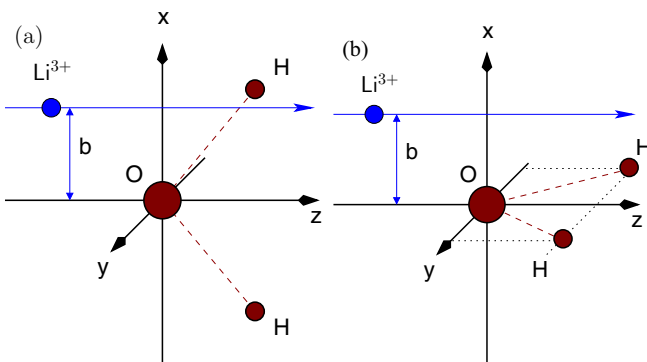


FIG. 2. Geometries of the Li^{3+} - H_2O collision system. (a) The collision plane and the molecular plane coincide. (b) The molecular plane is perpendicular to the collisional plane.

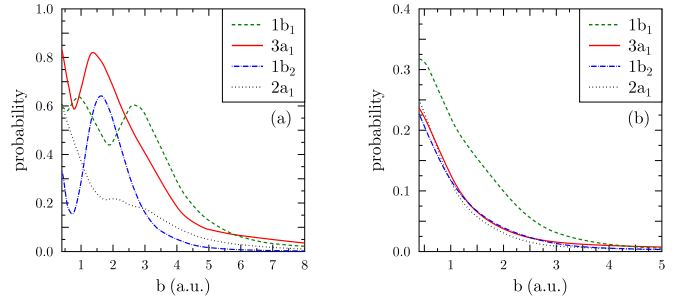


FIG. 3. Single-electron removal probabilities for the active MOs $\{1b_1, 3a_1, 1b_2, 2a_1\}$ as functions of the impact parameter for Li^{3+} - H_2O collisions at (a) $E_p = 20$ keV/u and (b) $E_p = 1000$ keV/u. The geometry corresponds to the configuration depicted in Fig. 2(b).

B. Cross-section analysis including modeling of Auger-electron emission

The TC-BGM IEM calculations yield single-electron transition amplitudes and probabilities to the bound states of the projectile and the target and to the (discretized) continuum. In Fig. 3, we show, as a function of the impact parameter for the orientation of Fig. 2(b) and the two projectile energies $E_p = 20$ keV/u [Fig. 3(a)] and $E_p = 1000$ keV/u [Fig. 3(b)], the total electron removal probabilities of the active MOs $\{1b_1, 3a_1, 1b_2, 2a_1\}$ obtained from summing up all capture and direct ionization contributions. Electron removal from the innermost $1a_1$ orbital is very weak and not considered.

At high projectile energies where electron capture is negligibly small, this geometry favors ionization from the highest occupied MO, $1b_1$, whose symmetry plane coincides with the collision plane. The electron removal probabilities from the other three orbitals are all sizable, but somewhat smaller and, at $E_p = 1000$ keV/u, similar to each other [Fig. 3(b)] despite the differences in binding energy ($\varepsilon_{3a_1} = -0.466$, $\varepsilon_{1b_2} = -0.624$, and $\varepsilon_{2a_1} = -1.285$ a.u. compared to $\varepsilon_{1b_1} = -0.403$ a.u. according to the self-consistent-field calculation of Ref. [54]). This is partly a geometry effect specific to the chosen configuration and partly a reflection of the well-known fact that ionization from more deeply bound orbitals gains importance toward high impact energies.

Figure 3(a) demonstrates that electron removal from the $2a_1$ orbital is substantial at $E_p = 20$ keV/u as well. In this region, electron capture dominates and can roughly be understood by comparing the initial-state and final-state binding energies. Given that $\varepsilon_{\text{Li}^{2+}(n=2)} = -1.125$ a.u. is close to ε_{2a_1} , the non-negligible $2a_1$ -removal probability is not surprising.

$2a_1$ -vacancy production in H_2O is followed by Auger-electron emission [46]. We conclude from Fig. 3 that this postcollision process may give sizable corrections to multiple-electron removal cross sections calculated within the IEM. In Ref. [55], a straightforward statistical model for estimating these corrections was proposed. Here we extend that model for q -fold removal in order to differentiate between direct ionization and electron-capture events.

We wish to calculate probabilities (and cross sections) for capture of k electrons accompanied by transitions of l electrons to the continuum (ionization) corresponding to the removal of $q = k + l$ electrons. In an IEM description in which Auger

processes (and the Pauli exclusion principle) are not taken into account, these probabilities are obtained from multinomial combinations of single-electron probabilities for capture, p_i^{cap} , and ionization, p_i^{ion} , from the i th MO [56]:

$$\begin{aligned}
 P_{kl}^{\text{no Auger}} &= \sum_{k_1, \dots, k_m=0}^{N_1, \dots, N_m} \sum_{l_1, \dots, l_m=0}^{N_1, \dots, N_m} \delta_{k, \sum_i k_i} \delta_{l, \sum_i l_i} \\
 &\times \prod_{i=1}^m \binom{N_i}{k_i + l_i} \binom{k_i + l_i}{k_i} \\
 &\times (p_i^{\text{cap}})^{k_i} (p_i^{\text{ion}})^{l_i} (1 - p_i^{\text{cap}} - p_i^{\text{ion}})^{N_i - k_i - l_i} \\
 &\equiv \sum_{k_1, \dots, k_m=0}^{N_1, \dots, N_m} \sum_{l_1, \dots, l_m=0}^{N_1, \dots, N_m} \delta_{k, \sum_i k_i} \delta_{l, \sum_i l_i} \tau(\dots). \quad (5)
 \end{aligned}$$

In Eq. (5), m is the number of active MOs, N_i is the number of electrons in the i th MO before the collision, and $\tau(\dots)$ in the last expression is a shorthand notation for the product of multinomial coefficients and single-electron probabilities. The Kronecker δ 's select those combinations of electrons captured (ionized) from the active MOs which contribute to a given overall number k (l) of captured (ionized) electrons. For the present case of H_2O targets, we have $m = 4$ and $N_i = 2$ for $i \in \{1b_1, 3a_1, 1b_2, 2a_1\}$. Multiplication of the probabilities (5) by and integration over the impact parameter yields the partial, charge-state-correlated cross sections

$$\sigma_{kl}^{\text{no Auger}} = 2\pi \int_0^\infty b P_{kl}^{\text{no Auger}}(b) db. \quad (6)$$

Consideration of Auger-electron emission involves the inclusion of correction probabilities. Let $\mathcal{P}(q_{2a_1}, n, \alpha)$ be the probability for the production of α additional electrons after direct removal of $q_{2a_1} = k_{2a_1} + l_{2a_1}$ electrons from $2a_1$ and $n = k_{1b_2} + l_{1b_2} + k_{3a_1} + l_{3a_1} + k_{1b_1} + l_{1b_1}$ electrons from the other MOs [55]. The probabilities for k -fold capture and simultaneous l -fold ionization are now given as

$$\begin{aligned}
 P_{kl}^{\text{Auger}} &= \sum_{k_{2a_1}, k_{1b_2}, k_{3a_1}, k_{1b_1}} \sum_{l_{2a_1}, l_{1b_2}, l_{3a_1}, l_{1b_1}} \sum_{\alpha} \\
 &\times \delta_{k, \sum_i k_i} \delta_{l, \sum_i (l_i + \alpha)} \mathcal{P}(q_{2a_1}, n, \alpha) \tau(\dots), \quad (7)
 \end{aligned}$$

where all of the sums run from 0 to 2 and the α Auger electrons contribute to the total number of l electrons in the continuum [cf. the second Kronecker δ in Eq. (7)]. The correction probabilities $\mathcal{P}(q_{2a_1}, n, \alpha)$ are calculated by strictly following Eqs. (4) and (5) of Ref. [55] and assuming that one Auger electron is produced with certainty if exactly one electron is removed from the $2a_1$ orbital and no electron from the other MOs. This results in

$$\mathcal{P}(q_{2a_1}, n, \alpha) = \begin{cases} 1 & \text{if } q_{2a_1} = \alpha = 0 \\ 0 & \text{if } q_{2a_1} = 0, \alpha > 0 \\ \frac{n}{6} & \text{if } q_{2a_1} = 1, \alpha = 0 \\ \frac{6-n}{6} & \text{if } q_{2a_1} = 1, \alpha = 1 \\ \frac{n^2}{36} & \text{if } q_{2a_1} = 2, \alpha = 0 \\ \frac{n(6-n)}{18} & \text{if } q_{2a_1} = 2, \alpha = 1 \\ \frac{(6-n)^2}{36} & \text{if } q_{2a_1} = 2, \alpha = 2, \end{cases} \quad (8)$$

which ensures that $\sum_{\alpha} \mathcal{P}(q_{2a_1}, n, \alpha) = 1$ for each number q_{2a_1} of vacancies in $2a_1$ and independently of the number n of electrons directly removed from the other MOs. If $n = 0$, then $\mathcal{P}(1, n, 1) = 1$, i.e., we recover the assumption that Auger emission happens with certainty if one vacancy is produced in $2a_1$. Similarly, we have $\mathcal{P}(2, 0, 2) = 1$, i.e., two-electron Auger emission happens for two vacancies in $2a_1$. On the other hand, if $n = 6$, then $\mathcal{P}(q_{2a_1}, n, \alpha > 0) = 0$, reflecting the fact that no outer-shell electrons are available for Auger emission. For intermediate cases, we have $0 < \mathcal{P}(q_{2a_1}, n, \alpha) < 1$, i.e., the model assumes that both Auger and radiative decays occur. Alternatively, one may assume that Auger-electron emission will always happen with certainty as long as outer-shell electrons are available. We have checked that this model variant does not result in significant changes in the partial, charge-state-correlated cross sections σ_{kl} . The insensitivity of the results to the details of the Auger model is due to the fact that those contributions in Eq. (7) that are affected by different assumptions involve products of relatively small probabilities.

In Fig. 4, we compare the σ_{kl} obtained from Eq. (7) together with Eq. (8) with those obtained from Eq. (5) in order to assess the role of Auger-electron emission. The cross sections are displayed as functions of impact energy for (a) pure ionization (PI) corresponding to $k = 0$, (b) single

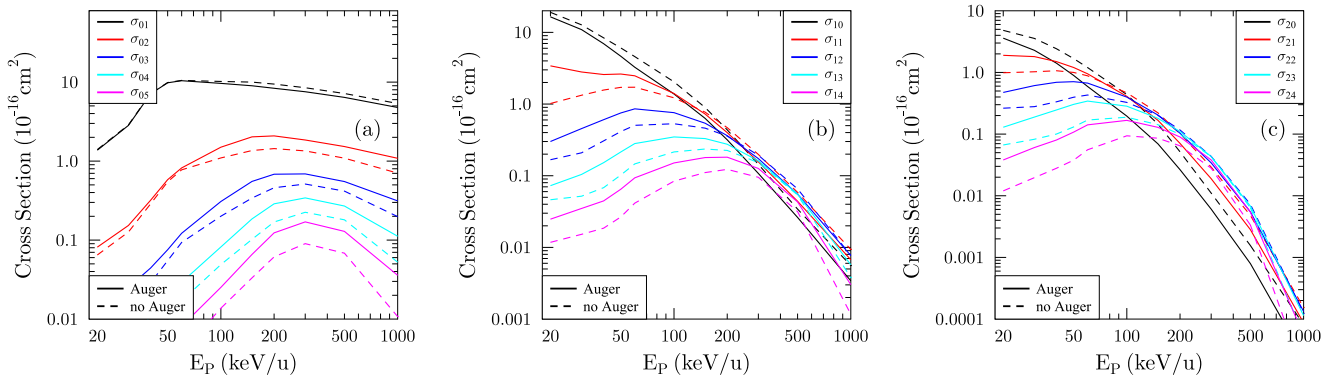


FIG. 4. Partial, charge-state-correlated cross sections σ_{kl} for k -fold capture and l -fold ionization as functions of impact energy for Li^{3+} - H_2O collisions: (a) pure ionization ($k = 0$), (b) single capture ($k = 1$), and (c) double capture ($k = 2$). Solid lines correspond to Eqs. (7) and (8), i.e., they include Auger processes, and dashed lines correspond to Eq. (5), i.e., Auger processes are ignored.

capture (SC) corresponding to $k = 1$, and (c) double capture (DC) corresponding to $k = 2$. The most obvious trend in all three cases is an overall reduction of the cross sections that involve the smallest number of electrons ($\sigma_{01}, \sigma_{10}, \sigma_{20}$), once Auger-electron emission is taken into account. These channels lose contributions to channels with higher l , since $2a_1$ vacancy production is associated with additional outer-shell ionization in the Auger case and cannot contribute to σ_{01}, σ_{10} , and σ_{20} . For the higher ionization multiplicities, both feeding and depletion due to Auger processes do occur and the redistribution of the total yield is, in general, more complicated. Nevertheless, for PI [Fig. 4(a)], we observe a clear pattern, namely all $\sigma_{0l}^{\text{Auger}}$ with $l \geq 2$ are larger than their no-Auger counterparts, e.g., at $E_p = 200$ keV/u by 40–100% when moving from $l = 2$ up to $l = 5$. This is a consequence of the fact that direct PI strictly decreases with increasing multiplicity l . As a consequence, the cross-section contribution that is moved, say, from σ_{01} to σ_{02} when Auger processes are switched on is larger than what is lost by σ_{02} to higher multiplicities.

In the case of electron capture, we observe the same trend at relatively low impact energies where pure capture ($l = 0$) dominates over transfer ionization ($l > 0$). The corrections due to Auger emission are sizable, e.g., σ_{11} is enhanced by about a factor of 3 at $E_p = 20$ keV/u [Fig. 4(b)]. Toward higher energies, pure capture decreases rapidly. At $E_p = 150$ keV/u, $\sigma_{10}^{\text{no Auger}} \approx \sigma_{11}^{\text{no Auger}}$ and feeding and depletion of the latter channel balance each other, i.e., the net effect of Auger emission on σ_{11} is close to zero. The trend reverses at even higher energies and overall is more pronounced for the DC channels where the depletion of, e.g., σ_{21} is already stronger than the feeding at around $E_p = 150$ keV/u [Fig. 4(c)].

IV. COMPARISON OF EXPERIMENTAL AND THEORETICAL RESULTS

A. Total single- and double-capture cross sections

For the following comparisons of experimental and theoretical cross sections, the effects of Auger-electron emission are always included in the calculations, i.e., Eqs. (7) and (8) are used. The total SC and DC cross sections, both of which include transfer-ionization contributions, are shown in Figs. 5 and 6, respectively. The experimental data are represented by the full-square symbols, while the theoretical results are represented by three sets of lines. The dashed curves correspond to the complete sums $\sum_l \sigma_{kl}$, while only up to three- and four-electron processes are included in the results depicted by the solid and dash-dotted curves, respectively. The experimental cross sections are obtained via the growth-rate method (see Sec. II A) and are absolute, i.e., they do not depend on any normalization procedure or detection-efficiency correction.

For total SC (Fig. 5), the overall agreement between theory and experiment is reasonable over the measured energy range, in particular when the sum over the degree of ionization is restricted. The fact that the complete sum results in cross sections which are somewhat larger than the experimental values at most energies reflects the well-known tendency of the IEM to overestimate higher degrees of ionization.

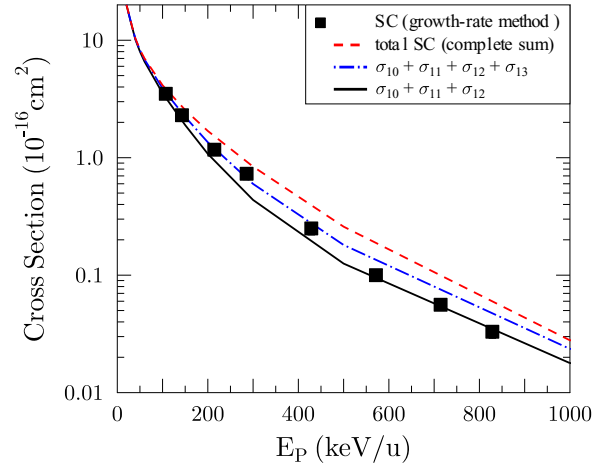


FIG. 5. Total single-capture (SC) cross section as a function of impact energy for $\text{Li}^{3+}\text{-H}_2\text{O}$ collisions. Experimental data (solid squares) are obtained via the growth-rate method. The error bars are smaller than the size of the symbols. Theory: the dashed line corresponds to the complete sum $\sum_l \sigma_{1l}$, the dash-dotted line to the restricted sum $\sigma_{10} + \sigma_{11} + \sigma_{12} + \sigma_{13}$, and the solid line to $\sigma_{10} + \sigma_{11} + \sigma_{12}$. The calculations include Auger-electron emission.

The total DC (Fig. 6) shows a similar trend. If we restrict the sum of the theoretical cross sections to the first two terms, we observe good agreement with the growth-rate measurements. The inclusion of calculated cross sections for higher degrees of ionization results in a (significant) overestimation of the experimental data, once again signaling the shortcomings of the IEM framework.

B. Partial, charge-state-correlated cross sections

The partial cross-sections differential in the final projectile and target charge states are shown in Figs. 7, 8, and 9 for PI

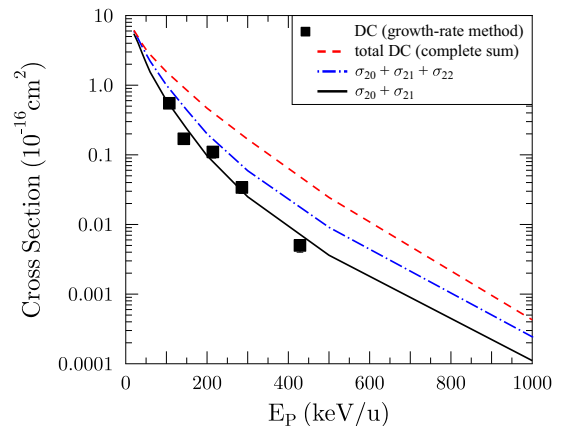


FIG. 6. Total double-capture (DC) cross section as a function of impact energy for $\text{Li}^{3+}\text{-H}_2\text{O}$ collisions. Experimental data (solid squares) are obtained via the growth-rate method. The error bars are smaller than the size of the symbols. Theory: the dashed line corresponds to the complete sum $\sum_l \sigma_{2l}$, the dash-dotted line to the restricted sum $\sigma_{20} + \sigma_{21} + \sigma_{22}$, and the solid line to $\sigma_{20} + \sigma_{21}$. The calculations include Auger-electron emission.

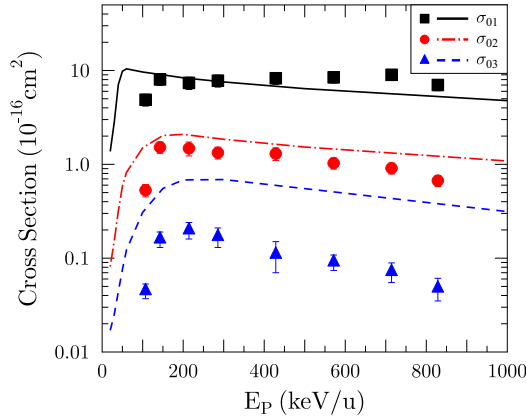


FIG. 7. Pure-ionization cross sections σ_{01} , σ_{02} , and σ_{03} as functions of impact energy for Li^{3+} - H_2O collisions. The symbols represent the experimental results (most error bars are smaller than the size of the symbols) and the lines represent the calculations (including Auger-electron emission).

(σ_{01} , σ_{02} , and σ_{03}), SC (σ_{10} , σ_{11} , and σ_{12}), and DC (σ_{20} , σ_{21} , and σ_{22}), respectively.

For a triply charged projectile, one would expect good agreement between an IEM calculation and experiment for processes that involve up to three electrons [57]. However, in Fig. 7, we observe good agreement only for pure single and double ionization (σ_{01} , σ_{02}), whereas the triple-ionization cross section σ_{03} appears to be overestimated by the calculation by a factor of 2 or more. This might signal an early breakdown of the IEM, but some experimental limitations have to be considered as well. As mentioned at the end of Sec. II B, the experimental setup is not able to distinguish $\text{H}^+ + \text{H}^+$ production from the production of just one proton. The former is always counted as a single event, causing two-electron removal processes that result in $\text{H}^+ + \text{H}^+ + \text{O}$ production to appear in the one-electron removal channels σ_{10} and σ_{01} . Likewise, three-electron removal giving rise to $\text{H}^+ +$

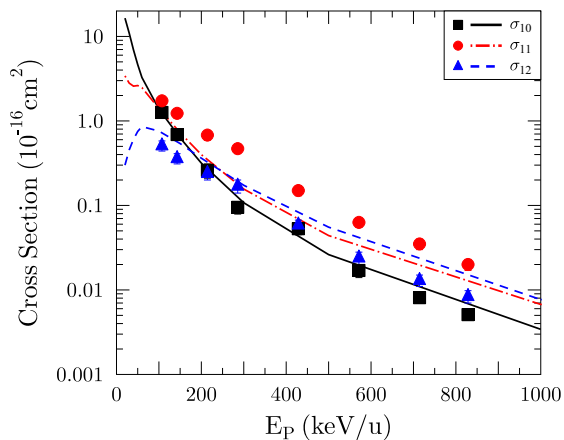


FIG. 8. Single capture cross sections σ_{10} , σ_{11} , and σ_{12} as functions of impact energy for Li^{3+} - H_2O collisions. The symbols represent the experimental results (most error bars are smaller than the size of the symbols) and the lines represent the calculations (including Auger-electron emission).

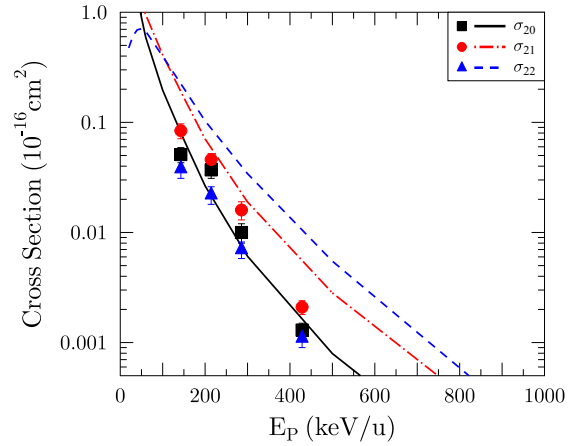


FIG. 9. Double-capture cross sections σ_{20} , σ_{21} , and σ_{22} as functions of impact energy for Li^{3+} - H_2O collisions. The symbols represent the experimental results and the lines represent the calculations (including Auger-electron emission).

$\text{H}^+ + \text{O}^+$ production appears in the two-electron removal channels σ_{20} , σ_{21} , and σ_{22} (and similarly for higher degrees of ionization).

This misidentification problem is deemed uncritical for σ_{01} , since the falsely included $\text{H}^+ + \text{H}^+ + \text{O}$ channel should be weak compared to the true single-ionization contributions, i.e., the contamination is expected to be minor. The multiple-ionization cross sections σ_{02} and σ_{03} might change more significantly if properly corrected. For σ_{03} , one may expect a significant enhancement from the missing $\text{H}^+ + \text{H}^+ + \text{O}^+$ events, which are falsely included in σ_{02} . On the other hand, the measured σ_{03} values are contaminated by $\text{H}^+ + \text{H}^+ + \text{O}^{2+}$ contributions. The latter are expected to be small compared to the $\text{H}^+ + \text{H}^+ + \text{O}^+$ channel such that the net effect of a proper correction will most likely be an increase of the experimental σ_{03} results and better agreement with the calculation. Unfortunately, it is currently not possible to quantify this.

For similar reasons, the experimental σ_{02} values would probably increase as well, if properly corrected for the misidentified channels: $\text{H}^+ + \text{H}^+ + \text{O}$ production, which would feed into σ_{02} from σ_{01} , should be larger than $\text{H}^+ + \text{H}^+ + \text{O}^+$ production, which is falsely included. Again, we cannot quantify the magnitude of this effect.

Moving on to the SC results displayed in Fig. 8, we note that the calculated pure SC cross section σ_{10} is in good agreement with the measurements, albeit slightly larger at high impact energies. Note that Auger-electron emission reduces σ_{10} [cf. Fig. 4(b)]. Had we not included this effect, we would have observed less satisfactory agreement between theoretical and experimental results.

The most striking feature of Fig. 8 is the dominance of the transfer-ionization channels over pure SC. According to the measurements, σ_{11} is by far the strongest channel at all impact energies. It is followed by σ_{12} , except at the three lowest-energy values where σ_{10} is stronger. According to the calculation, σ_{12} is even stronger than σ_{11} for most of the displayed impact energy range, which is in part a consequence of taking Auger-electron emission into account. Comparing Fig. 4(b) with Fig. 8 indicates, however, that the strong discrepancy

between the theoretical and experimental σ_{11} values cannot be explained by the Auger effect.

The repercussions of the experimental misidentification problem on the SC channels are difficult to assess. One point that can be made is that the measured σ_{10} is contaminated by $H^+ + H^+ + O$ events and should be smaller than it appears in Fig. 8. Depending on the magnitude of the contamination, this can have a detrimental effect on the comparison with the calculation. The transfer-ionization channels σ_{11} and σ_{12} are both fed and depleted by misidentified events, as are their PI counterparts σ_{01} and σ_{02} . But unlike the latter, the SC channels are not ordered in magnitude according to the degree of ionization. This makes it impossible to predict whether the overall effect of the contaminations is an increase or a decrease of σ_{11} and σ_{12} . In any case, it seems unlikely that correction of this experimental problem would significantly improve the comparison with theory.

In Fig. 9, we present the partial DC cross sections. For pure DC σ_{20} , the agreement between experiment and theory is good, and for σ_{21} , it is still acceptable at intermediate energies. Both calculated cross sections are reduced by the inclusion of Auger processes above $E_p \approx 100$ – 150 keV/u [cf. Fig. 4(c)], which improves the agreement with the data. In contrast, σ_{22} is strongly overestimated by the calculation (with and without inclusion of the Auger effect). This was to be expected from the total DC results shown in Fig. 6 and is consistent with the limitations of the IEM for higher electron multiplicities. Again, the experimental misidentifications might change these comparisons, but we expect the disagreement for σ_{22} to persist.

C. Perturbative vs nonperturbative regime

One important task in the study of molecular and atomic ionization is to assess whether ionization processes occur within the perturbative collision regime. If the ionization process can be described using first-order theories, one can,

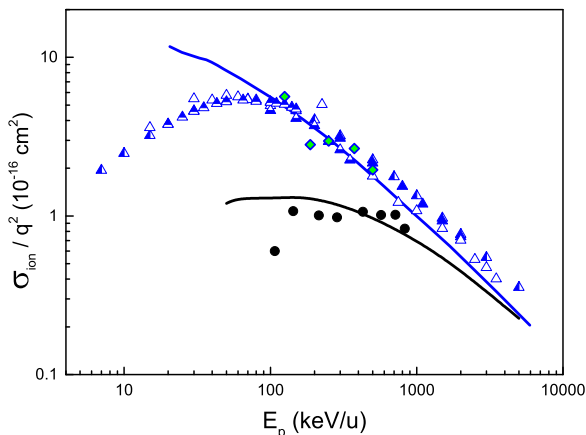


FIG. 10. Pure total ionization cross section $\sum_l \sigma_{0l}$ divided by the squared projectile charge q^2 as a function of impact energy for H_2O targets. Experimental data: black circles - Li^{3+} (present work), triangles - H^+ : left filled [4], bottom filled [5], top filled [6], open [7], and full [9]. Calculations: black line - Li^{3+} (present work), blue line Refs. [36–38].

e.g., extrapolate the cross sections toward higher velocities or look at scaling properties with respect to the projectile charge state q . A prominent example for this is the q^2 scaling rule being satisfied for the PI cross sections. This is an indication that in this regime, distant collisions dominate the ionization process [58].

Figure 10 shows experimental data and calculations for total PI of H_2O . The plotted quantity is $\sum_{l=1}^3 \sigma_{0l}/q^2$ for Li^{3+} and protons (experimental data are from Refs. [4–7] and theoretical calculations from Refs. [36–38]) and for He^+ (experimental data from Ref. [15]). The tendency toward a universal, charge-independent scaling law at high energies is similar to what was found for neon-target ionization induced by the same projectiles in the same energy range [42]. In both cases, neon and water, the q^2 scaling rule seems to be fulfilled at energies above 1000 keV/u. On the other hand, at lower velocities, the discrepancy from the q^2 scaling reaches a factor of ~ 5 . We can conclude that for collisions within the energy range studied in this work, simple first-order theories cannot be used and more sophisticated theoretical approaches such as the TC-BGM must be applied.

V. CONCLUSIONS

Pure-ionization and single- and double-capture cross sections were measured for Li^{3+} impact on H_2O molecules in the energy range from 0.75 to 5.8 MeV. The results were compared to TC-BGM IEM calculations coupled with Auger-electron emission after vacancy production in the $2a_1$ molecular orbital. The results show good overall agreement between theory and experiment for the total single capture and for pure single and double ionization.

Cross sections for higher degrees of ionization are typically overestimated by the calculations, which points to limitations of the IEM framework. Inclusion of the Auger effect improves the agreement with the experimental data, notably for the capture channels $\sigma_{10}, \sigma_{20}, \sigma_{21}$, but unexplained factor of 2–3 discrepancies were observed for the transfer-ionization channel σ_{11} .

The experimental methodology used is unable to distinguish the production of a single H^+ from simultaneous $H^+ + H^+$ production. This problem impeded the comparison of theoretical and experimental charge-state-correlated cross sections for higher multiplicities, particularly in the capture channels, in which the cross sections are not ordered in magnitude according to the degree of ionization. It is important to point out that the detection of two simultaneous protons is not a straightforward experimental task. It would, however, be important to achieve such a measurement in order to shed more light on these multiple-electron removal processes and the ability and limitations of the IEM to describe them.

ACKNOWLEDGMENTS

This work was supported by the Brazilian agencies Fundação Carlos Chagas Filho de Amparo à Pesquisa do Estado do Rio de Janeiro and Conselho Nacional de Desenvolvimento Científico e Tecnológico, and by the

Natural Sciences and Engineering Research Council of Canada (NSERC) under Grant No. RGPIN-2014-03611. We thank

Mitsuko Murakami for contributions at an early stage of this project.

-
- [1] W. P. Levin, H. Kooy, J. S. Loeffler, and T. F. DeLaney, *Brit. J. Cancer* **93**, 849 (2005).
- [2] A. R. Smith, *Phys. Med. Biol.* **51**, R491 (2006).
- [3] D. Schardt, T. Elsässer, and D. Schulz-Ertner, *Rev. Mod. Phys.* **82**, 383 (2010).
- [4] M. E. Rudd, T. V. Goffe, R. D. DuBois, and L. H. Toburen, *Phys. Rev. A* **31**, 492 (1985).
- [5] U. Werner, K. Beckord, J. Becker, and H. O. Lutz, *Phys. Rev. Lett.* **74**, 1962 (1995).
- [6] F. Gobet, S. Eden, B. Coupier, J. Tabet, B. Farizon, M. Farizon, M. J. Gaillard, M. Carre, S. Ouaskit, T. D. Mark, and P. Scheier, *Phys. Rev. A* **70**, 062716 (2004).
- [7] H. Luna, A. L. F. de Barros, J. A. Wyer, S. W. J. Scully, J. Lecointre, P. M. Y. Garcia, G. M. Sigaud, A. C. F. Santos, V. Senthil, M. B. Shah, C. J. Latimer, and E. C. Montenegro, *Phys. Rev. A* **75**, 042711 (2007).
- [8] S. W. J. Scully, J. A. Wyer, V. Senthil, and M. B. Shah, and E. C. Montenegro, *Phys. Rev. A* **73**, 040701(R) (2006).
- [9] A. C. Tavares, H. Luna, W. Wolff, and E. C. Montenegro, *Phys. Rev. A* **92**, 032714 (2015).
- [10] L. H. Toburen and W. E. Wilson, *J. Chem Phys.* **66**, 5202 (1977)
- [11] F. Alvarado, R. Hoekstra, and T. Schlathölder, *J. Phys. B: At. Mol. Opt. Phys.* **38**, 4085 (2005).
- [12] A. L. F. de Barros, J. Lecointre, H. Luna, M. B. Shah, and E. C. Montenegro, *Phys. Rev. A* **80**, 012716 (2009).
- [13] S. Martin, L. Chen, R. Brédy, J. Bernard, and A. Cassimi, *J. Chem. Phys.* **142**, 094306 (2015)
- [14] M. E. Rudd, T. V. Goffe, and A. Itoh, *Phys. Rev. A* **32**, 2128 (1985).
- [15] P. M. Y. Garcia, G. M. Sigaud, H. Luna, A. C. F. Santos, E. C. Montenegro, and M. B. Shah, *Phys. Rev. A* **77**, 052708 (2008).
- [16] B. Sereidyuk, R. W. McCullough, H. Tawara, H. B. Gilbody, D. Bodewits, R. Hoekstra, A. G. G. M. Tielens, P. Sobocinski, D. Pesic, R. Hellhammer, B. Sulik, N. Stolterfoht, O. Abu-Haija, and E. Y. Kamber, *Phys. Rev. A* **71**, 022705 (2005).
- [17] R. Cabrera-Trujillo, E. Deumens, Y. Öhrn, O. Quinet, J. R. Sabin, and N. Stolterfoht, *Phys. Rev. A* **75**, 052702 (2007).
- [18] P. Sobocinski, Z. D. Pešić, R. Hellhammer, N. Stolterfoht, B. Sulik, S. Legendre, and J.-Y. Chesnel, *J. Phys. B: At. Mol. Opt. Phys.* **38**, 2495 (2005).
- [19] P. Sobocinski, Z. D. Pešić, R. Hellhammer, D. Klein, B. Sulik, J.-Y. Chesnel, and N. Stolterfoht, *J. Phys. B: At. Mol. Opt. Phys.* **39**, 927 (2006).
- [20] Z. D. Pešić, R. Hellhammer, B. Sulik, and N. Stolterfoht, *J. Phys. B: At. Mol. Opt. Phys.* **42**, 235202 (2009).
- [21] Z. D. Pešić, J.-Y. Chesnel, R. Hellhammer, B. Sulik, and N. Stolterfoht, *J. Phys. B: At. Mol. Opt. Phys.* **37**, 1405 (2004).
- [22] S. Legendre, E. Giglio, M. Tarisien, A. Cassimi, B. Gervais, and L. Adoui, *J. Phys. B: At. Mol. Opt. Phys.* **38**, L233 (2005).
- [23] C. Dal Cappello, C. Champion, O. Boudrioua, H. Lekadir, Y. Sato, and D. Ohsawa, *Nucl. Instrum. Methods Phys. Res. B* **267**, 781 (2009).
- [24] S. Nandi, S. Biswas, A. Khan, J. M. Monti, C. A. Tachino, R. D. Rivarola, D. Misra, and L. C. Tribedi, *Phys. Rev. A* **87**, 052710 (2013).
- [25] D. Bodewits and R. Hoekstra, *Phys. Rev. A* **76**, 032703 (2007).
- [26] H. Luna and E. C. Montenegro, *Phys. Rev. Lett.* **94**, 043201 (2005).
- [27] E. C. Montenegro, M. B. Shah, H. Luna, S. W. J. Scully, A. L. F. Barros, J. A. Wyer, and J. Lecointre, *Phys. Rev. Lett.* **99**, 213201 (2007).
- [28] G. H. Olivera, C. Caraby, P. Jardin, A. Cassimi, L. Adoui, and B. Gervais, *Phys. Med. Biol.* **43**, 2347 (1998).
- [29] S. Otranto, R. E. Olson, and P. Beiersdorfer, *J. Phys. B: At. Mol. Opt. Phys.* **40**, 1755 (2007).
- [30] L. F. Errea, Clara Illescas, L. Méndez, B. Pons, I. Rabadán, and A. Riera, *Phys. Rev. A* **76**, 040701(R) (2007).
- [31] Clara Illescas, L. F. Errea, L. Méndez, B. Pons, I. Rabadán, and A. Riera, *Phys. Rev. A* **83**, 052704 (2011).
- [32] L. F. Errea, Clara Illescas, L. Méndez, and I. Rabadán, *Phys. Rev. A* **87**, 032709 (2013).
- [33] T. Liamsuwan and H. Nikjoo, *Phys. Med. Biol.* **58**, 641 (2013).
- [34] C. Champion, O. Boudrioua, C. Dal Cappello, Y. Sato, and D. Ohsawa, *Phys. Rev. A* **75**, 032724 (2007).
- [35] H. J. Lüdde, T. Spranger, M. Horbatsch, and T. Kirchner, *Phys. Rev. A* **80**, 060702(R) (2009).
- [36] M. Murakami, T. Kirchner, M. Horbatsch, and H. J. Lüdde, *Phys. Rev. A* **85**, 052704 (2012).
- [37] M. Murakami, T. Kirchner, M. Horbatsch, and H. J. Lüdde, *Phys. Rev. A* **85**, 052713 (2012).
- [38] M. Murakami, T. Kirchner, M. Horbatsch, and H. J. Lüdde, *Phys. Rev. A* **86**, 022719 (2012).
- [39] J. E. Miraglia and M. S. Gravielle, *Phys. Rev. A* **81**, 042709 (2010).
- [40] C. C. Montanari, E. C. Montenegro, and J. E. Miraglia, *J. Phys. B* **43**, 165201 (2010).
- [41] W. Wolff, H. Luna, A. C. F. Santos, E. C. Montenegro, R. D. DuBois, C. C. Montanari, and J. E. Miraglia, *Phys. Rev. A* **84**, 042704 (2011).
- [42] J. S. Ihani, H. Luna, W. Wolff, and E. C. Montenegro, *J. Phys. B* **46**, 115208 (2013).
- [43] G. Schenk and T. Kirchner, *Phys. Rev. A* **91**, 052712 (2015).
- [44] J. Suárez, L. Méndez, and I. Rabadán, *J. Phys. Chem. Lett.* **6**, 72 (2015).
- [45] K. H. Tan, C. E. Brion, Ph. E. Van Der Leeuw, and M. J. Van Der Leeuw, *Chem. Phys.* **29**, 299 (1978).
- [46] E. C. Montenegro, *J. Phys.: Conf. Ser.* **194**, 012049 (2009).
- [47] W. Wolff, I. J. de Souza, A. C. Tavares, G. F. S. de Oliveira, and H. Luna, *Rev. Sci. Instrum.* **83**, 123107 (2012).
- [48] H. Tawara and A. Russek, *Rev. Mod. Phys.* **45**, 178 (1973).
- [49] W. Wolff, H. Luna, A. C. F. Santos, E. C. Montenegro, and G. M. Sigaud, *Phys. Rev. A* **80**, 032703 (2009).
- [50] I. Ben-Itzhak, S. G. Ginther, and K. D. Carnes, *Phys. Rev. A* **47**, 2827 (1993).
- [51] E. G. Cavalcanti, G. M. Sigaud, E. C. Montenegro, M. M. SantAnna, and H. Schmidt-Böcking, *J. Phys. B* **35**, 3937 (2002).

- [52] E. G. Cavalcanti, G. M. Sigaud, E. C. Montenegro, and H. Schmidt-Böcking, *J. Phys. B* **36**, 3087 (2003).
- [53] T. Kirchner, M. Murakami, M. Horbatsch, and H. J. Lüdde, *Adv. Quantum Chem.* **65**, 315 (2013).
- [54] S. Aung, R. M. Pitzer, and S. I. Chan, *J. Chem. Phys.* **49**, 2071 (1968).
- [55] T. Spranger and T. Kirchner, *J. Phys. B* **37**, 4159 (2004).
- [56] M. Horbatsch, *Phys. Lett. A* **187**, 185 (1994).
- [57] G. Schenk, M. Horbatsch, and T. Kirchner, *Phys. Rev. A* **88**, 012712 (2013).
- [58] V. A. Sidorovich, V. S. Nikolaev, and J. H. McGuire, *Phys. Rev. A* **31**, 2193 (1985).